

Large-Scale Computational Identification of p-Type Oxide Semiconductors by Hierarchical Screening

Yong Youn,^{†,||} Miso Lee,^{†,||} Doyeon Kim,[†] Jae Kyeong Jeong,[‡] Youngho Kang,^{*,§} and Seungwu Han^{*,†}

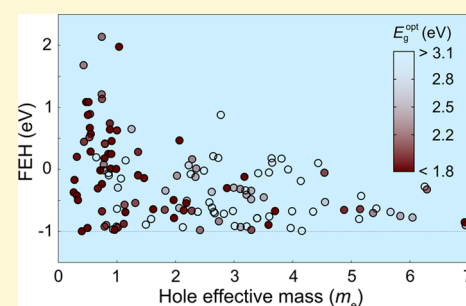
[†]Department of Materials Science and Engineering and Research Institute of Advanced Materials, Seoul National University, Seoul 08826, Korea

[‡]Department of Electronic Engineering, Hanyang University, Seoul 04763, Korea

[§]Materials Data Center, Korea Institute of Materials Science, Changwon 51508, Korea

Supporting Information

ABSTRACT: With potentials to outperform traditional semiconductors, oxide semiconductors are penetrating into a wide range of energy, environmental, and electronic applications. However, an insufficient library of p-type oxides is a major obstacle against complete oxide electronics. To identify promising p-type oxides, we carry out a large-scale computational screening over 17,700 oxygen-containing compounds using the hydrogen descriptor that was shown to select the p-type oxide reliably. To enable high-throughput screening, we use in the initial stage coarse but simple descriptors that correlate with the hydrogen descriptor. Through a hierarchical screening procedure, we find 156 p-type oxides with the band gap larger than 1.1 eV, discovering promising candidates such as NaNbO_2 and $\text{La}_2\text{SiO}_4\text{Se}$ and also new types of p-type oxides. Furthermore, we classify the identified p-type oxides according to the valence-band character and reveal chemical principles underlying the p-type dopability.



INTRODUCTION

Owing to the tunable property, high stability, and standardized fabrication process, oxides have become key materials in almost every electronic and energy application.^{1–4} In particular, oxide semiconductors possessing band gaps of 1–4 eV with controllable carrier densities and high mobilities have potentials to overcome cost, performance, and process limitations of authoritative semiconductors such as Si and GaAs.^{1,5} As such, they are rapidly penetrating into a wide range of applications encompassing sensors,⁶ catalysts,⁷ solar cells,⁸ as well as electronic^{1,5,9} and optoelectronic¹⁰ devices. For example, transistors utilizing In-based amorphous oxides are used in high-end commercial displays,¹¹ and oxide-based p–n diodes have engendered a high-density stackable memory.¹² Furthermore, the wide band gap in many oxides enables transparent electronics that envision captivating applications such as smart windows and transparent displays.^{9,11}

A critical obstacle in the current oxide electronics is the absence of good p-type oxide semiconductors; well-known p-type oxides such as NiO ,¹³ SnO ,¹⁴ and Cu_2O ¹⁵ are poor in performance or stability when compared to n-type counterparts such as ZnO ,² In_2O_3 ,¹⁶ and Ga_2O_3 .¹⁷ Because of this deficiency, practical implementations of oxide semiconductors are confined to unipolar device structures. Development of high-performance p-type components would greatly expand the application area of oxide semiconductors by permitting, for

example, energy efficient devices^{1,18} or sensors with new functionalities.⁶

The fundamental reason underlying the scarcity of p-type oxides is well understood:¹⁹ the valence band of oxides is relatively low in energy and made of localized oxygen p orbitals, which makes the material prone to hole compensation caused by donor-like defects and increases the hole effective mass. Such basic restrictions necessitate testing a large number of candidate materials to find the optimal ones. Inspired by this, several groups attempted to identify promising p-type transparent oxides or chalcogenides via high-throughput screening based on the density-functional theory (DFT) calculations.^{20–26}

In every theoretical screening for p-type materials, the first step is to define relevant descriptors. The optical transparency can be readily assessed by the direct gap, and the hole effective mass is a reasonable descriptor for carrier mobilities, although several factors contribute to the mobility. Trickier is the p-type dopability, which is essentially related to the energy position of valence bands. The branch-point energy can be a measure of the p-type tendency,^{22,24,26,27} but we recently showed that this descriptor does not well distinguish the n-type and p-type oxide groups.²³ Alternatively, we suggested a reliable descriptor

Received: February 27, 2019

Revised: July 6, 2019

Published: July 9, 2019

for the p-type dopability based on the formation energy of hydrogen impurity (FEH) and found that every known p-type oxide satisfies the condition of $\text{FEH} > -1$ eV. FEH captures the energy cost of the electron transfer from hydrogen to the valence band maximum (VBM) and thus correlates well with the valence band position.²³

Although FEH is a solid descriptor for p-type dopability, it requires significant computational efforts due to defect calculations, severely limiting the screening pool. As such, we were able to scan over only 94 oxides in ref 23 that were selected based on the known chemistry of p-type oxides. Screening over a broader material space can potentially reveal more promising materials and/or a new class of p-type oxides. In this work, to identify p-type oxide semiconductors that can be used in electronic devices, we carry out a large-scale screening over a vast material space. This is enabled by finding two coarse but simple descriptors, the band gap and the proportion of O-p orbitals to the valence band, which correlate with FEH. Using the computational data accessible in AFLOW,²⁸ we screen over 17,700 oxygen-containing compounds and select 426 compounds for the calculation of FEH. Finally, we identify 156 oxide semiconductors with the band gap larger than 1.1 eV and good p-type dopability.

METHODS

DFT Calculations. We perform high-throughput DFT calculations using Vienna Ab initio Simulation Package.^{29,30} Various procedures of DFT calculations, namely, convergence tests, geometry optimization, and electronic structure calculations, are handled automatically by the Automated Ab initio Modeling of Materials Properties Package (AMP²).^{31,32} The exchange-correlation energy of electrons is calculated within the PBE functional.³³ For 3d orbitals in transition metal elements (V-Zn), we apply on-site Coulomb interactions, so called the PBE + U method, with U values from ref 34. Throughout this work, the spin-polarized calculations are performed with initially ferromagnetic spin alignment. In calculations that require accurate band gaps, we use a hybrid HSE06 functional³⁵ with a quarter fraction of the exact exchange energy. To compute the band gap with the hybrid functional, we apply the approach in the previous work.³² This method identifies the k -points at the band extrema within PBE and then evaluates the band energy at these points using the hybrid functional. The hole effective mass is calculated by following the same method as in ref 23. In this method, the effective mass is averaged over the reciprocal space, considering the Fermi–Dirac occupation at 300 K when the Fermi level lies at the valence top. This averaged mass is a more relevant descriptor than a value at the band extremum for the transport properties if the materials have nonparabolic band structures. The second derivative of the electron energy with respect to k -points in the effective mass calculation is computed using the finite-difference method on a very fine k -point grid with the spacing of $0.04\pi/\text{\AA}$ between k -points. When using $0.02\pi/\text{\AA}$ of the k -point space for test materials, we find only small variations in effective masses (within 7% compared to the results with $0.04\pi/\text{\AA}$).

FEH. FEH is the energy cost to form the interstitial hydrogen defect in the +1 charge state when the Fermi level lies at VBM, which is calculated according to the following formula

$$\text{FEH} = E(\text{H}_i^+) - E(\text{clean}) - \mu_{\text{H}} + E_{\text{V}} \quad (1)$$

where E is the energy of supercells, μ_{H} is the chemical potential of hydrogen, and E_{V} indicates the energy level of VBM. For μ_{H} , we assume a hydrogen-rich condition, which sets μ_{H} to one-half of the total energy of the H_2 molecule. Since the full hybrid-functional calculation of FEHs is very expensive, we first evaluate FEH using the PBE functional (FEH_{PBE}) and correct the position of VBM and overbinding in the O–H bond²³

$$\text{FEH} = \text{FEH}_{\text{PBE}} + \Delta\text{VBM} - 0.27 \text{ eV} \quad (2)$$

where ΔVBM is the difference in VBM between PBE(+ U) and HSE06 calculations.³⁶

Defect Calculations. For notable candidate materials, we carry out full defect calculations to confirm the p-type tendency and suggest possible sources of hole carriers. Since the band gap should be described accurately for obtaining accurate defect properties, we use the HSE06 functional. The spurious electrostatic interactions between charged defects are lifted by the Freysoldt, Neugebauer, and Van de Walle (FNV) scheme,³⁷ which was extended for anisotropic systems in ref 38. The static dielectric tensor for the FNV correction is obtained from the density functional perturbation theory within PBE. The chemical potentials are bound by the phase stability of a given material in consideration of possible secondary phases from the Materials Project database.³⁹

RESULTS AND DISCUSSION

Simple Descriptors for p-Type Oxides. Although FEH is a reliable descriptor for p-type dopability, it requires sheer computational loads from defect calculations, which limit the material space for screening. To enable large-scale high-throughput calculations, it is necessary to find descriptors that are simpler than FEH but still correlate well with FEH. To this end, we first examine correlations between FEH and various elemental or bulk properties that can be easily accessed by theory or experiment. The considered properties include elemental information⁴⁰ for metal species such as electronegativity (EN_{M}), work function (W_{M}), oxidation state (OS_{M}), and ionization energy (IE_{M}) and structural information such as the average coordination number of oxygen (CN_{O}) and metal ions (CN_{M}) in the crystal. (OS_{M} is determined by pinning the valency of oxygen to -2 .) We also include computational results on the crystalline structure such as band gaps obtained using PBE ($E_{\text{g}}^{\text{PBE}}$) or hybrid functionals ($E_{\text{g}}^{\text{HSE}}$), oxygen partial weight at VBM (w_{O} ; see below), and hole effective mass (m_{h}^*). We obtain w_{O} using the density of states (DOS) as follows

$$w_{\text{O}} = \frac{\int_{E_{\text{V}}-\delta}^{E_{\text{V}}} D_{\text{O}}(E) dE}{\int_{E_{\text{V}}-\delta}^{E_{\text{V}}} D(E) dE} \quad (3)$$

where $D(E)$ and $D_{\text{O}}(E)$ denote the total DOS and projected DOS onto oxygen p orbitals, respectively, and δ is set to 0.5 eV.

Using Pearson correlation coefficient matrix (PCCM), we first investigate the correlations for 54 stable binary oxides encompassing various metal species. The magnitudes of PCCM are displayed in Figure 1a. When calculated over all the oxides (see upper-left triangles), w_{O} , OS_{M} , and IE_{M} strongly correlate with FEH, while $E_{\text{g}}^{\text{PBE}}$, $E_{\text{g}}^{\text{HSE}}$, m_{h}^* , and CN_{O} exhibit weak but meaningful correlations. However, if the test oxides are limited to those with $\text{FEH} > -2$ eV (18 oxides) that are likely to be p-type, magnitudes of correlation coefficients for $E_{\text{g}}^{\text{PBE}}$, $E_{\text{g}}^{\text{HSE}}$, and m_{h}^* become higher than for OS_{M} , IE_{M} , and CN_{O} . Considering that $E_{\text{g}}^{\text{PBE}}$ and $E_{\text{g}}^{\text{HSE}}$ are highly correlated, we choose w_{O} , $E_{\text{g}}^{\text{PBE}}$, and m_{h}^* as candidate descriptors for FEH.

Next, we test predictability of the selected descriptors (w_{O} , $E_{\text{g}}^{\text{PBE}}$, and m_{h}^*) for FEH using the receiver-operating-characteristic (ROC) analysis (see Figure 1b). The dataset is augmented with 67 ternary compounds that the previous work identified as potential p-type oxides²³ and with randomly chosen 52 ternary oxides (in total, 173 oxides). The ROC analysis evaluates a descriptor for binary classification by adjusting the distinction threshold. To obtain the ROC curve, we group

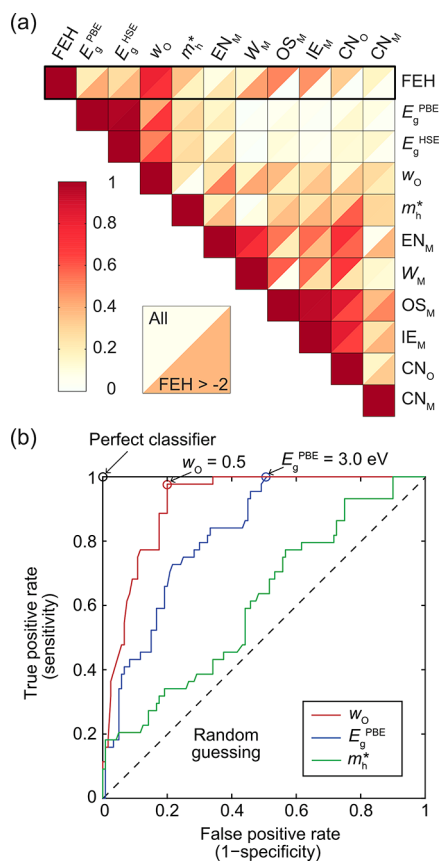


Figure 1. (a) Pearson correlation coefficient matrix of potential descriptors and FEH. Upper and lower triangles indicate the magnitude of coefficients over 54 binary oxides and those with $\text{FEH} > -2$ eV, respectively. (b) Receiver-operating-characteristic curves of w_{O} , $E_{\text{g}}^{\text{PBE}}$, and m_{h}^* for binary classification of p-type materials.

oxides with $\text{FEH} > -1$ eV as positive samples and the rest as negative ones. We then evaluate the true- and false-positive rates (TPR and FPR, respectively), which correspond to sensitivity and $1 - \text{specificity}$, respectively, while adjusting the threshold (t_{TH}) of the descriptors. The TPR (FPR) is a ratio of the number of samples that are correctly (falsely) classified as positive samples to the total number of positive (negative) samples during the test. Thus, the point in the ROC plot for a perfect classifier is located at the left-top corner, that is, the (0,1) coordinate. On the other hand, the classification purely relying on a random guess results in a point along the $y = x$ line (the dashed line in Figure 1b).

Figure 1b shows that, since w_{O} , $E_{\text{g}}^{\text{PBE}}$, and m_{h}^* have negative correlations with FEH, the ROC curves approach one for TPR as t_{TH} decreases, while FPR increases to some extent. w_{O} is a good descriptor because the ROC curve appears at the left-top corner. Similarly, $E_{\text{g}}^{\text{PBE}}$ can also serve as a reasonable descriptor. However, the ROC curve of m_{h}^* is similar to the random-guessing line. The good correlations of w_{O} and $E_{\text{g}}^{\text{PBE}}$ with FEH can be rationalized as follows: O-p orbitals are inherently low in energy; therefore, the low value of w_{O} signifies the presence of other orbitals above O-p, possibly increasing the valence band energy. In the case of $E_{\text{g}}^{\text{PBE}}$, the wide band gap tends to push down the valence band in energy. Therefore, we choose w_{O} and $E_{\text{g}}^{\text{PBE}}$ as coarse descriptors for FEH, with the decision boundary of $w_{\text{O}} = 0.5$ and $E_{\text{g}}^{\text{PBE}} = 3$ eV (see Figure S1 for more details).

Screening over a Large Database of Oxides. Figure 2 illustrates the screening strategy for p-type oxides schemati-

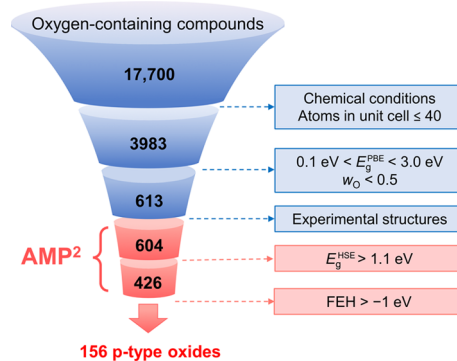


Figure 2. Screening procedure for identifying p-type oxides.

cally. In the initial stage, we exploit computational data in the AFLOW database that provides DOS and energy gap at the PBE(+ U) level.²⁸ Furthermore, partial DOS projected on each atomic orbital is also available in the database, which allows for estimating w_{O} according to eq 3.

The computational methods used in AFLOW are largely equivalent to those in the present work, except that AFLOW applied the PBE + U method to most d-block elements, while we apply U only to 3d metals. For most elements, differences in the result are negligible, but for noble metals such as Ag, Pd, Pt, and Au, the U values in AFLOW are rather high, which tends to increase w_{O} in the corresponding compounds. This makes well-known p-type materials such as AgAlO_2 filtered out, and therefore, we use our own PBE (without U) results on w_{O} and $E_{\text{g}}^{\text{PBE}}$ for these noble-metal compounds (see Figure S2 and Table S1 for comparison of w_{O} between the present work and AFLOW).

The AFLOW database provides 17,700 oxygen-containing compounds (as of 21 November 2017) that exist in the International Crystal Structure Database (ICSD).⁴¹ Among them, we first select materials based on the chemical formula: (i) Compounds without metal elements are excluded. (ii) We rule out compounds including halogen elements or polyatomic anions that consist of C, N, P, S, Se, and O such as $(\text{SO}_4)^{2-}$, $(\text{PO}_4)^{3-}$, $(\text{NO}_3)^-$, $(\text{CO}_3)^{2-}$, and $(\text{P}_2\text{O}_7)^{4-}$ because they usually result in lower FEHs than pure oxides because of higher electronegativities. For instance, SnO has an FEH of 0.65 eV, while FEH of $\text{Sn}(\text{SO}_4)$ is -0.64 eV. (iii) Among lanthanides and actinides, we only consider those including La and Ac because of chemical similarities within the period. Additionally, we omit large primitive cells that contain more than 40 atoms to enable high-throughput calculations. This stage also removes structural duplicates.

The first step reduces the candidate materials by more than fourfold. The next stage screens materials based on the coarse descriptor for FEH, as discussed in the previous section, selecting materials that satisfy $w_{\text{O}} < 0.5$ and $0.1 \text{ eV} < E_{\text{g}}^{\text{PBE}} < 3$ eV. The lower bound for $E_{\text{g}}^{\text{PBE}}$ is set to exclude metallic compounds from being selected. Here, we intend to include small-gap oxides because they could be useful in electronic devices that do not require transparency. These DFT-based filters reduce the candidate p-type oxides down to 613. Next, by referring to ICSD, we select 604 oxides that were identified experimentally. We then compute $E_{\text{g}}^{\text{HSE}}$ and select 426 compounds with $E_{\text{g}}^{\text{HSE}}$ larger than 1.1 eV, the energy gap of

Si, which considers the current controllability when used in transistor devices. Finally, we compute FEHs and select those with FEH > -1 eV, resulting in 156 candidate p-type oxides.

Figure 3 shows FEH and averaged E_g^{HSE} of the final p-type candidates. (18 materials with the hole effective mass bigger

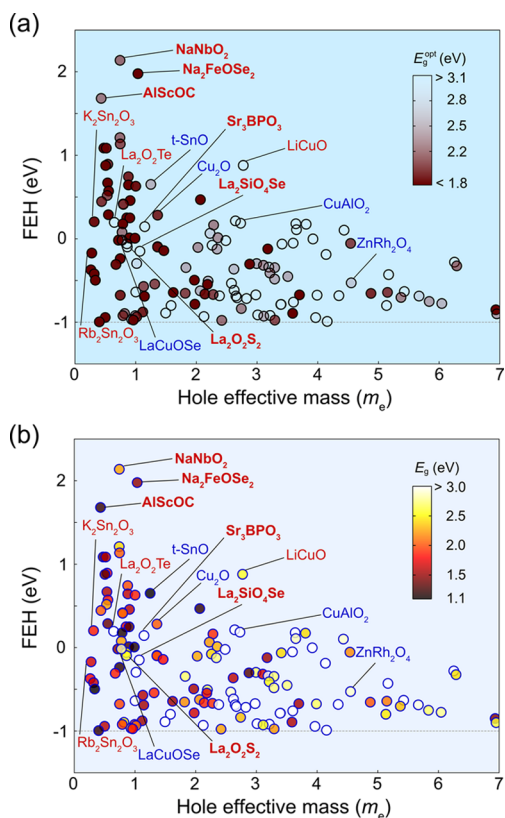


Figure 3. Distribution of FEHs and hole effective masses of the final candidate p-type oxides. Each material is filled with color according to the (a) optical and (b) fundamental band gaps, respectively. Compositions of notable p-type oxides are shown in color as follows: blue, experimentally known; red, suggested in previous theoretical screenings; red and bold, newly identified in the present work.

than $7 m_e$ are not displayed.) SnO with a tetragonal crystal structure has 0.7 eV of the band gap, which is smaller than 1.1 eV, but we include it in Figure 3 (see t-SnO) because it is an archetypal p-type oxide. Each material is colored according to the optical gap (Figure 3a) or the fundamental gap (Figure 3b). The full list of candidates is presented in Tables S2–S7.

Notable p-Type Oxide Semiconductors. First of all, candidate materials in Figure 3 include most of oxides that are known to be p-type experimentally. The well-known p-type oxides such as t-SnO, Cu_2O , ZnRh_2O_4 , CuAlO_2 ,⁴³ and LaCuOSe ⁴⁴ are marked in blue (see below for the full list). However, some binary p-type oxides such as NiO, CuO ,⁴⁵ MnO ,⁴⁶ and CoO ⁴⁷ are missing because they were filtered in the second stage utilizing w_0 and E_g^{PBE} ; w_0 of NiO is 0.66, and other transition metal oxides are metallic because of band-gap underestimation in PBE combined with incorrect spin ordering (ferromagnetic calculation despite the antiferromagnetic ground state). Nevertheless, FEH of these materials with antiferromagnetic spin ordering satisfies the present criterion of p-type dopability (NiO: -0.52 eV; CuO : -0.87 eV; MnO : -0.37 eV; CoO : 0.08 eV). Figure 3 also identifies candidate materials suggested in the previous screening such as $\text{La}_2\text{O}_2\text{Te}$,

$\text{K}_2\text{Sn}_2\text{O}_3$, and LiCuO (marked in red).^{20,23} Meanwhile, several candidates proposed in earlier works are filtered because of low FEHs (-1.08 eV of $\text{La}_2\text{O}_2\text{Se}_2$ ²² and -1.25 eV of $\text{K}_2\text{Pb}_2\text{O}_3$ ²⁰) or inclusion of halogen elements ($\text{Sb}_4\text{Cl}_2\text{O}_5$ ²⁰). (We find that FEH of $\text{Sb}_4\text{Cl}_2\text{O}_5$ is -1.73 eV, lower than -1.66 eV for Sb_2O_3 .) In below, we remark on the notable materials in Figure 3 that have not been reported to be p-type experimentally nor highlighted clearly in previous computational screenings.

NaNbO_2 ($P6_3/mmc$) shows the highest FEH among oxides we investigated, suggesting facile doping. Combined with the small hole effective mass ($0.74 m_e$), NaNbO_2 is expected to display high p-type conductivity. Figure 4a shows the atomic structure of NaNbO_2 where Na, O, and Nb layers alternate along the z-direction. As shown in Figure 4b, Nb-d states form VBM separated from the oxygen p-band, resulting in a high FEH. The two-dimensional nature results in anisotropic hole effective masses between in-plane ($0.59 m_e$) and out-of-plane ($1.43 m_e$) directions. Formation energies of various point defects are shown in Figure 4c. We find that sodium vacancy (V_{Na}) can play as an acceptor with a low formation energy. Its charge transition level appears at 0.2 eV above VBM, which is shallower than for Cu vacancies in Cu^{1+} -bearing oxides.^{48,49} Therefore, V_{Na} may serve as an intrinsic source of hole carriers. The negative formation energy of V_{Na} may originate from inconsistency in the functional between the chemical-potential boundary (the phase diagram in Materials Project database using the PBE functional) and defect energies (HSE functional).

The oxychalcogenide $\text{La}_2\text{SiO}_4\text{Se}$ (Figure 4d) looks promising as a transparent semiconducting oxide with a wide band gap (3.82 eV), together with FEH (-0.15 eV) and effective mass ($1.07 m_e$) comparable to those of known p-type oxides. The Se-4p states dominating the valence band top raise VBM and reduce hole effective mass in a planar direction, as can be seen in Figure 4e (Se atoms exist only on certain layers as shown in Figure 4d). The defect energies in Figure 4f indicate that undoped $\text{La}_2\text{SiO}_4\text{Se}$ may have low hole concentrations due to compensation by V_{Se} . However, Ca doping at the La site (Ca_{La}) could be a hole source with shallow (0/-) transition level (0.17 eV) and the low formation energy.

Other notable materials in Figure 3 are $\text{Na}_2\text{FeOSe}_2$, $\text{La}_2\text{O}_2\text{S}_2$, AlScOC , and Sr_3BPO_3 . Among them, $\text{Na}_2\text{FeOSe}_2$ has the second highest FEH (1.97 eV) and low hole effective mass ($1.04 m_e$) with the ferromagnetic ordering. However, FEH drops to -0.18 eV on antiferromagnetic ordering, which is slightly more stable than the ferromagnetic structure by 17 meV/atom. (The hole effective mass is $1.15 m_e$.) This is because the energy position of the valence band is sensitive to the exchange splitting. The magnetism-dependent p-type property would be an intriguing topic that merits future investigation. On the other hand, $\text{La}_2\text{O}_2\text{S}_2$, AlScOC , and Sr_3BPO_3 are multi-anion compounds with a non-oxygen anion (S, C, and P) (see Figures S3–S5 for more details). Like Se in $\text{La}_2\text{SiO}_4\text{Se}$, outer p-orbitals of these anions mainly form VBM, resulting in high FEHs. $\text{La}_2\text{O}_2\text{S}_2$ ($Cmce$) would be interesting in application to a transparent (semi)conductor because of its moderate effective mass ($0.86 m_e$) and large optical band gap (3.12 eV). The defect formation energies of $\text{La}_2\text{O}_2\text{S}_2$ in Figure S3 show that Ca doping could generate sufficient hole concentrations.

For actual applications, the identified candidates may need to endure harsh device-fabrication conditions such as high temperatures and low pressures. In the case of NaNbO_2 and

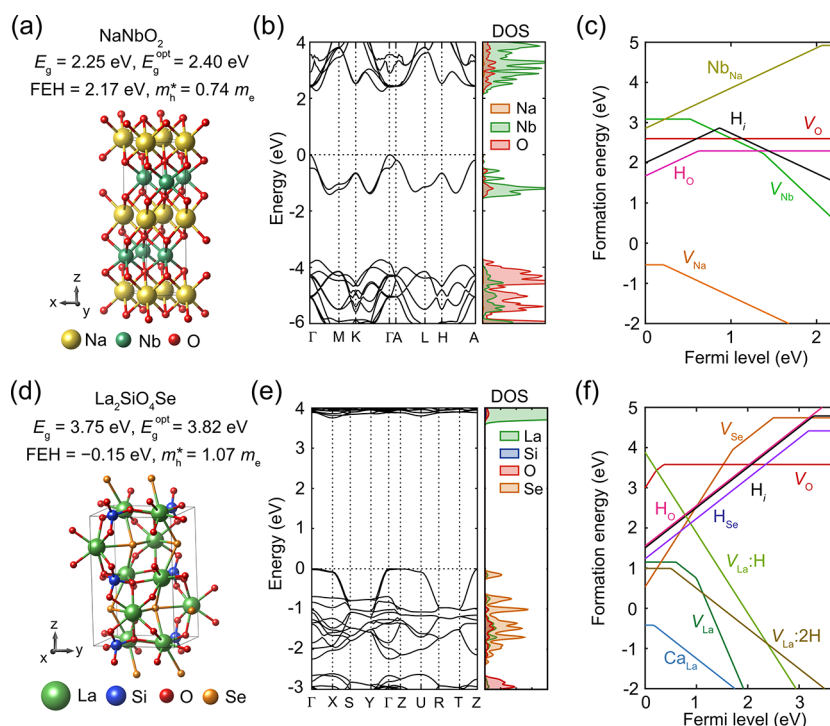


Figure 4. (a) Crystal structure, (b) band structure and partial density of states (VBM is set to 0), and (c) formation energies of native and hydrogen-related defects of NaNbO_2 . (d) Crystal structure, (e) band structure and partial density of states, and (f) formation energies of native, hydrogen-related and Ca_{La} defects of $\text{La}_2\text{SiO}_4\text{Se}$. Band structures in (b) and (e) are obtained using PBE calculations with scissor corrections to match with the HSE gaps. For (c) and (f), oxygen-rich conditions are assumed.

$\text{La}_2\text{SiO}_4\text{Se}$, highlighted as notable p-type oxides, their single crystals were grown at >1000 K and found to exist stably at room temperature.^{50,51} This indicates that these oxides are likely to retain their crystal forms at conventional process temperatures of electronic devices (<800 K).¹ On the other hand, several vacuum processes would be involved during the fabrication of devices, but the stability of NaNbO_2 and $\text{La}_2\text{SiO}_4\text{Se}$ under such low-pressure conditions has not been fully verified yet. However, in light of the fact that films of a broad range of oxide semiconductors such as InGaZnO_4 , ZnO , and Cu_2O have been successfully synthesized through vacuum deposition techniques,¹ we expect that low-pressure conditions do not critically hamper the synthesis of the proposed p-type oxides.

Classification of p-Type Candidates. As mentioned in Introduction, oxides are rarely p-type mainly because of O-p orbitals occupying VBM. Therefore, the identified p-type materials can be classified by the type of orbitals that defy the dominance of O-p characters at the valence top. Thus, Figure 5a categorizes the candidates into three groups according to orbital characters of VBM. It is intriguing that this classification emerges by theoretical inspection only, but it is largely consistent with the empirical design principles of p-type oxides.^{43,52,53}

As is known in Cu^{1+} - or Rh^{3+} -bearing oxides, the VBM position in Group-I oxides rises by hybridization with filled d states in transition metals that are high in energy. Group I constitutes the majority of candidates (110 out of 156), and we divide them into three subgroups depending on the occupancy of d shells (see Figure 5b–d). In the first subgroup (Figure 5b), d electrons are unpaired like Nb^{3+} in NaNbO_2 . This applies to many transition metal ions such as V^{3+} , Cr^{3+} , Mn^{2+} , Fe^{2+} , Co^{2+} , Nb^{3+} , and W^{4+} . Transition metals in the second

subgroup (Figure 5c) adopt the low spin configuration of d^6 or d^8 , resulting in quasi-closed d shells under the crystal field splitting. A well-known p-type oxide in this category is ZnRh_2O_4 in the spinel structure where Rh^{3+} forms an octahedral complex with the low-spin d^6 configuration.⁴² In Figure 5c, we identify ternary Pd^{2+} - or Pt^{2+} -bearing oxides, which is a new class of p-type oxides as far as we are aware. These oxides contain the square planar complex in low spin d^8 configurations. Last, the third subgroup consists of Cu^{1+} - and Ag^{1+} -bearing oxides with d^{10} configurations (see Figure 5d). Most materials in this subgroup include Cu^{1+} , and their p-type behaviors are well established.

Hole effective masses of Group-I oxides are significantly affected by the principal quantum number of d orbital; the average value of hole effective masses is the highest ($9.39 m_e$) for oxides with 3d characters of valence bands, while it reduces to $3.44 m_e$ for 4d and $1.53 m_e$ for 5d characters. This tendency originates from the different spatial extent among nd states ($n = 3, 4, \text{ and } 5$); the nd states are spatially more extended with increasing n, which enhances the hybridization between orbitals of adjacent transition metals.

Similar to Group-I oxides, valence bands of Group-II oxides in Figure 5e are dominated by cationic states, but in this case, the metal s orbital couples with the O-p states. The well-known t-SnO belongs to this group. The chemical diversity is narrow in Group II compared to other groups, encompassing only six oxides: SnO , $\text{K}_2\text{Sn}_2\text{O}_3$, $\text{Rb}_2\text{Sn}_2\text{O}_3$, $\text{In}_7\text{IrGeO}_8$, $\text{In}_6\text{Ge}_2\text{PtO}_9$, and $\text{In}_6\text{Ga}_2\text{PtO}_8$. (Here, SnO has an orthorhombic crystal structure with E_g^{HSE} of 1.95 eV. $\text{K}_2\text{Sn}_2\text{O}_3$ has cubic or rhombohedral structures.) This is understandable because weakly bound electrons in the outer s orbital easily transfer to anions, and empty s orbitals form the conduction band. One exception is Sn with the valence configuration of $5s^25p^2$; it is the most

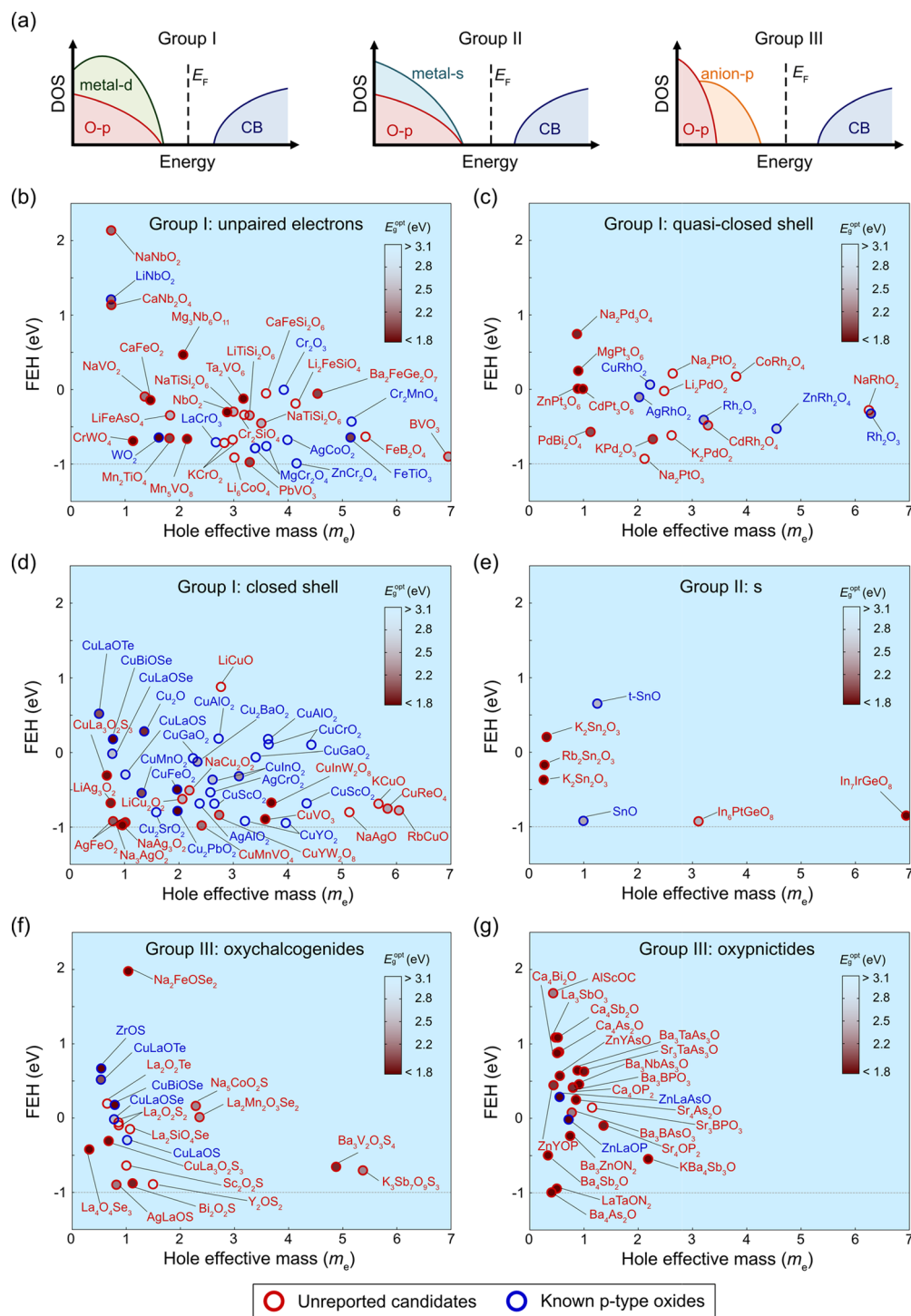


Figure 5. (a) Three distinct orbital characteristics at the valence top in the identified p-type oxides. (b)–(g) FEH and hole effective mass of the candidates: (b) Group I, unpaired electrons; (c) Group I, quasi-closed shell d^6 (Rh^{3+}) or d^8 (Pd^{2+} and Pt^{2+}); (d) Group I, closed shell d^{10} (Cu^{1+} and Ag^{1+}); (e) Group II, s; (f) Group III, oxychalcogenides; (g) Group III, oxypnictides. The data for AlScOC, the only oxycarbide identified in the present work, is presented in (g). The color code inside each data indicates the optical band gap. The compositions of reported p-type oxides are colored in blue, while unreported ones are marked in red. Cu^{1+} -bearing oxychalcogenides appear in both (d) and (f).

stable in Sn^{4+} but also can exist in the metastable Sn^{2+} with occupied s states forming VBM. In addition to Sn^{2+} -bearing oxides, several oxides such as PbO and Bi_2O_3 have a closed s orbital from Pb^{2+} or Bi^{3+} , and therefore, they might be p-type dopable. However, both oxides are not predicted to be p-type in the present screening because of low FEHs (PbO: -1.32 eV; Bi_2O_3 : -1.62 eV). Indeed, PbO and Bi_2O_3 were reported

with mainly n-type characters.^{54,55} On the other hand, In with Ss^2Sp^1 valence electrons usually become an In^{3+} ion in oxides, and the empty Ss orbital contributes to the conduction band. However, for In_7IrGeO_8 , $In_6Ge_2PtO_9$, and $In_6Ga_2PtO_8$ in Group II, the In s character is found to be dominant at VBM. This occurs because In atoms bond with neighboring Pt or Ir atoms covalently, which prevents the full ionization of In. In

light of this finding, the covalent bond between cations would become a new design principle for p-type oxides.

Unlike Groups I and II, Group-III oxides such as LaCuOSe, which records the highest p-type conductivity among oxides up to date, contain multi-anions with chalcogen (Figure 5f) or pnictogen (Figure 5g) elements. Owing to the spatially extended, high-energy p states of non-oxygen anions, these materials can have higher valence bands than for pure oxides, displaying high FEHs. Owing to the large size of outer orbitals of non-oxygen anions, many Group-III oxides have light hole effective masses ($\sim 1 m_e$ or less). Thus, the facile hole transport is expected for this group of oxides. Overall, oxychalcogenides exhibit larger band gaps and heavier hole effective masses than oxypnictides. This is attributed to higher degrees of localization and deeper energy in outer orbitals of chalcogen elements than for the pnictogen group.

One may wonder if there are specific applications particularly suitable for a certain oxide group. However, as shown in Figure 5, physical properties of candidates are quite scattered even within the same group. Thus, it would be difficult to specify applications for a certain oxide group. Instead, we can suggest material-specific applications considering detailed properties of candidates. For example, in each group, there are several potential candidates for application to a transparent (semi)conductor, for example, La₂O₂Te (Group III), LiCuO (Group I), La₂SiO₄Se (Group III), and La₂O₂S₂ (Group III). Among them, the first two have been suggested in the previous study for the same application.²³ On the other hand, all the candidates identified in the present work possess larger band gaps than Si. Thus, they would hold promise as a channel in transistor devices, yielding advantages over Si in the breakdown voltage and leakage current. In addition, the two polymorphs of K₂SnO₃ (Group II) and ZnYOP (Group III) and LaTa₂N₂O (Group III) are of particular interest because they exhibit small effective masses less than 0.5 m_e and band gaps larger than for Si by ~ 0.5 eV.

CONCLUSIONS

In summary, we introduced a high-throughput protocol for discovering new p-type oxide semiconductors. By evaluating the correlation between FEH and the elemental information, we identified two coarse but simple descriptors: the band gap and oxygen partial weights at VBM. By applying these descriptors to the AFLOW database and carrying out our own high-throughput calculations of FEH, we were able to screen as many as 17,700 oxygen-containing compounds. As a result, we identified 156 p-type candidates and suggest promising candidates including NaNbO₂ and La₂SiO₄Se and new types of p-type oxides. Additionally, we classified the p-type candidates according to their orbital character at the valence band, revealing chemical principles underlying p-type oxides. We believe that the present list of candidate p-type oxides will be very useful in selecting optimal oxides in diverse applications.

ASSOCIATED CONTENT

Supporting Information

The Supporting Information is available free of charge on the ACS Publications website at DOI: 10.1021/acs.chemmater.9b00816.

FEH versus w_O and E_g^{PBE} plots; comparison of w_O between by HSE and by PBE; the unit-cell structure,

band structure, density of states, and defect formation energies diagram for the candidates La₂O₂S₂, AlScOC, and Sr₃BPO₃; and fundamental and optical gaps and hole effective masses of candidates in Figure 5b–f (PDF)

AUTHOR INFORMATION

Corresponding Authors

*E-mail: thehoya84@gmail.com (Y.K.)

*E-mail: hansw@snu.ac.kr (S.H.)

ORCID

Yong Youn: 0000-0003-3924-1373

Jae Kyeong Jeong: 0000-0003-3857-1039

Youngho Kang: 0000-0003-4532-0027

Author Contributions

Y.Y. and M.L. contributed equally to this work. The manuscript was written through contributions of all authors. All authors have given approval to the final version of the manuscript.

Notes

The authors declare no competing financial interest.

ACKNOWLEDGMENTS

This work was supported by Samsung Research Funding Center for Future Technology through Samsung Electronics. Y.K. acknowledges the Fundamental Research Program (no. PNK6410) of the Korea Institute of Materials Science, Republic of Korea. The computations were carried out at the KISTI Supercomputing Center (KSC-2018-CHA-0038).

REFERENCES

- (1) Fortunato, E.; Barquinha, P.; Martins, R. Oxide Semiconductor Thin-Film Transistors: A Review of Recent Advances. *Adv. Mater.* **2012**, *24*, 2945–2986.
- (2) Hoffman, R. L.; Norris, B. J.; Wager, J. F. ZnO-Based Transparent Thin-Film Transistors. *Appl. Phys. Lett.* **2003**, *82*, 733–735.
- (3) Cui, J.; Wang, A.; Edleman, N. L.; Ni, J.; Lee, P.; Armstrong, N. R.; Marks, T. J. Indium Tin Oxide Alternatives—High Work Function Transparent Conducting Oxides as Anodes for Organic Light-Emitting Diodes. *Adv. Mater.* **2001**, *13*, 1476–1480.
- (4) Nomura, K.; Ohta, H.; Ueda, K.; Kamiya, T.; Hirano, M.; Hosono, H. Thin-Film Transistor Fabricated in Single-Crystalline Transparent Oxide Semiconductor. *Science* **2003**, *300*, 1269–1272.
- (5) Nomura, K.; Ohta, H.; Takagi, A.; Kamiya, T.; Hirano, M.; Hosono, H. Room-Temperature Fabrication of Transparent Flexible Thin-Film Transistors Using Amorphous Oxide Semiconductors. *Nature* **2004**, *432*, 488–492.
- (6) Kim, H.-J.; Lee, J.-H. Highly Sensitive and Selective Gas Sensors Using p-Type Oxide Semiconductors: Overview. *Sens. Actuators, B* **2014**, *192*, 607–627.
- (7) Liang, Y.; Li, Y.; Wang, H.; Zhou, J.; Wang, J.; Regier, T.; Dai, H. Co₃O₄ Nanocrystals on Graphene as a Synergistic Catalyst for Oxygen Reduction Reaction. *Nat. Mater.* **2011**, *10*, 780–786.
- (8) Jose, R.; Thavasi, V.; Ramakrishna, S. Metal Oxides for Dye-Sensitized Solar Cells. *J. Am. Ceram. Soc.* **2009**, *92*, 289–301.
- (9) Lorenz, M.; Ramachandra Rao, M. S.; Venkatesan, T.; Fortunato, E.; Barquinha, P.; Branquinho, R.; Salgueiro, D.; Martins, R.; Carlos, E.; Liu, A.; et al. The 2016 Oxide Electronic Materials and Oxide Interfaces Roadmap. *J. Phys. D: Appl. Phys.* **2016**, *49*, 433001.
- (10) Yu, X.; Marks, T. J.; Facchetti, A. Metal Oxides for Optoelectronic Applications. *Nat. Mater.* **2016**, *15*, 383–396.

- (11) Ide, K.; Nomura, K.; Hosono, H.; Kamiya, T. Electronic Defects in Amorphous Oxide Semiconductors: A Review. *Phys. Status Solidi* **2019**, 1800372.
- (12) Lee, M.-J.; Park, Y.; Kang, B.; Ahn, S.; Lee, C.; Kim, K.; Xianyu, W.; Stefanovich, G.; Lee, J.-H.; Chung, S.; et al. 2-Stack 1D-1R Cross-Point Structure with Oxide Diodes as Switch Elements for High Density Resistance RAM Applications. *IEEE Int. Electron Devices Meet.* **2007**, 771–774.
- (13) Sato, H.; Minami, T.; Takata, S.; Yamada, T. Transparent Conducting *p*-Type NiO Thin Films Prepared by Magnetron Sputtering. *Thin Solid Films* **1993**, 236, 27–31.
- (14) Caraveo-Frescas, J. A.; Nayak, P. K.; Al-Jawhari, H. A.; Granato, D. B.; Schwingenschlög, U.; Alshareef, H. N. Record Mobility in Transparent *p*-Type Tin Monoxide Films and Devices by Phase Engineering. *ACS Nano* **2013**, 7, 5160–5167.
- (15) Nagai, H.; Suzuki, T.; Hara, H.; Mochizuki, C.; Takano, I.; Honda, T.; Sato, M. Chemical Fabrication of *p*-Type Cu₂O Transparent Thin Film Using Molecular Precursor Method. *Mater. Chem. Phys.* **2012**, 137, 252–257.
- (16) Minami, T. New *n*-Type Transparent Conducting Oxides. *MRS Bull.* **2000**, 25, 38–44.
- (17) Pearton, S. J.; Yang, J.; Cary, P. H., IV; Ren, F.; Kim, J.; Tadjer, M. J.; Mastro, M. A. A Review of Ga₂O₃ materials, Processing, and Devices. *Appl. Phys. Rev.* **2018**, 5, No. 011301.
- (18) Martins, R.; Nathan, A.; Barros, R.; Pereira, L.; Barquinha, P.; Correia, N.; Costa, R.; Ahnood, A.; Ferreira, I.; Fortunato, E. Complementary Metal Oxide Semiconductor Technology With and On Paper. *Adv. Mater.* **2011**, 23, 4491–4496.
- (19) Banerjee, A. N.; Chattopadhyay, K. K. Recent Developments in the Emerging Field of Crystalline *p*-Type Transparent Conducting Oxide Thin Films. *Prog. Cryst. Growth Charact. Mater.* **2005**, 50, 52–105.
- (20) Hautier, G.; Miglio, A.; Ceder, G.; Rignanese, G.-M.; Gonze, X. Identification and Design Principles of Low Hole Effective Mass *p*-Type Transparent Conducting Oxides. *Nat. Commun.* **2013**, 4, 2292.
- (21) Bhatia, A.; Hautier, G.; Nilgianskul, T.; Miglio, A.; Sun, J.; Kim, H. J.; Kim, K. H.; Chen, S.; Rignanese, G.-M.; Gonze, X.; et al. High-Mobility Bismuth-Based Transparent *p*-Type Oxide from High-Throughput Material Screening. *Chem. Mater.* **2016**, 28, 30–34.
- (22) Sarmadian, N.; Saniz, R.; Partoens, B.; Lamoën, D. Easily Doped *p*-Type, Low Hole Effective Mass, Transparent oxides. *Sci. Rep.* **2016**, 6, 20446.
- (23) Yim, K.; Youn, Y.; Lee, M.; Yoo, D.; Lee, J.; Cho, S. H.; Han, S. Computational Discovery of *p*-Type Transparent Oxide Semiconductors Using Hydrogen Descriptor. *npj Comput. Mater.* **2018**, 4, 17.
- (24) Woods-Robinson, R.; Broberg, D.; Faghaninia, A.; Jain, A.; Dwaraknath, S. S.; Persson, K. A. Assessing High-Throughput Descriptors for Prediction of Transparent Conductors. *Chem. Mater.* **2018**, 30, 8375–8389.
- (25) Varley, J. B.; Miglio, A.; Ha, V. A.; Van Setten, M. J.; Rignanese, G. M.; Hautier, G. High-Throughput Design of Non-Oxide *p*-Type Transparent Conducting Materials: Data Mining, Search Strategy, and Identification of Boron Phosphide. *Chem. Mater.* **2017**, 29, 2568–2573.
- (26) Kormath Madam Raghupathy, R.; Wiebeler, H.; Kühne, T. D.; Felser, C.; Mirhosseini, H. Database Screening of Ternary Chalcogenides for *p*-type Transparent Conductors. *Chem. Mater.* **2018**, 30, 6794–6800.
- (27) Robertson, J.; Clark, S. J. Limits to Doping in Oxides. *Phys. Rev. B* **2011**, 83, No. 075205.
- (28) Curtarolo, S.; Setyawan, W.; Wang, S.; Xue, J.; Yang, K.; Taylor, R. H.; Nelson, L. J.; Hart, G. L. W.; Sanvito, S.; Buongiorno-Nardelli, M.; et al. AFLOWLIB.ORG: A Distributed Materials Properties Repository from High-Throughput Ab Initio Calculations. *Comput. Mater. Sci.* **2012**, 58, 227–235.
- (29) Kresse, G.; Furthmüller, J. Efficient Iterative Schemes for Ab Initio Total-Energy Calculations Using a Plane-Wave Basis Set. *Phys. Rev. B* **1996**, 54, 11169–11186.
- (30) Kresse, G.; Furthmüller, J. Efficiency of Ab-Initio Total Energy Calculations for Metals and Semiconductors Using a Plane-Wave Basis Set. *Comput. Mater. Sci.* **1996**, 6, 15–50.
- (31) Automated Ab initio Modeling of Materials Property Package. <https://www.snumat.com/packages/amp2> or <https://github.com/MDIL-SNU/AMP2> (accessed November 22, 2017).
- (32) Yim, K.; Yong, Y.; Lee, J.; Lee, K.; Nahm, H.-H.; Yoo, J.; Lee, C.; Seong Hwang, C.; Han, S. Novel High- κ Dielectrics for next-Generation Electronic Devices Screened by Automated Ab Initio Calculations. *NPG Asia Mater.* **2015**, 7, No. e190.
- (33) Perdew, J. P.; Burke, K.; Ernzerhof, M. Generalized Gradient Approximation Made Simple. *Phys. Rev. Lett.* **1996**, 77, 3865–3868.
- (34) Wang, L.; Maxisch, T.; Ceder, G. Oxidation Energies of Transition Metal Oxides within the GGA+U Framework. *Phys. Rev. B* **2006**, 73, 195107.
- (35) Heyd, J.; Scuseria, G. E.; Ernzerhof, M. Hybrid Functionals Based on a Screened Coulomb Potential. *J. Chem. Phys.* **2003**, 118, 8207–8215.
- (36) Park, S.; Lee, B.; Jeon, S. H.; Han, S. Hybrid Functional Study on Structural and Electronic Properties of Oxides. *Curr. Appl. Phys.* **2011**, 11, S337–S340.
- (37) Freysoldt, C.; Neugebauer, J.; Van de Walle, C. G. Fully Ab Initio Finite-Size Corrections for Charged-Defect Supercell Calculations. *Phys. Rev. Lett.* **2009**, 102, No. 016402.
- (38) Kumagai, Y.; Oba, F. Electrostatics-Based Finite-Size Corrections for First-Principles Point Defect Calculations. *Phys. Rev. B* **2014**, 89, 195205.
- (39) Jain, A.; Ong, S. P.; Hautier, G.; Chen, W.; Richards, W. D.; Dacek, S.; Cholia, S.; Gunter, D.; Skinner, D.; Ceder, G.; et al. Commentary: The Materials Project: A Materials Genome Approach to Accelerating Materials Innovation. *APL Mater.* **2013**, 1, No. 011002.
- (40) Lide, D. R. *CRC Handbook of Chemistry and Physics*; 86th Edition; CRC Press: FL, 2005.
- (41) FIZ Karlsruhe Inorganic Crystal Structure Database, available at: <http://icsd.fiz-karlsruhe.de> (accessed January 13, 2019).
- (42) Mizoguchi, H.; Hirano, M.; Fujitsu, S.; Takeuchi, T.; Ueda, K.; Hosono, H. ZnRh₂O₄: A *p*-Type Semiconducting Oxide with a Valence Band Composed of a Low Spin State of Rh³⁺ in a 4d⁶ Configuration. *Appl. Phys. Lett.* **2002**, 80, 1207–1209.
- (43) Kawazoe, H.; Yasukawa, M.; Hyodo, H.; Kurita, M.; Yanagi, H.; Hosono, H. *p*-Type Electrical Conduction in Transparent Thin Films of CuAlO₂. *Nature* **1997**, 389, 939–942.
- (44) Hiramatsu, H.; Ueda, K.; Ohta, H.; Hirano, M.; Kamiya, T.; Hosono, H. Degenerate *p*-Type Conductivity in Wide-Gap LaCuOS_{1-x}Se_x (x=0–1) Epitaxial Films. *Appl. Phys. Lett.* **2003**, 82, 1048–1050.
- (45) Shen, Y.; Guo, M.; Xia, X.; Shao, G. Role of Materials Chemistry on the Electrical/Electronic Properties of CuO Thin Films. *Acta Mater.* **2015**, 85, 122–131.
- (46) Crevecoeur, C.; De Wit, H. J. Electrical Conductivity of Li Doped MnO. *J. Phys. Chem. Solids* **1970**, 31, 783–791.
- (47) Bosman, A. J.; Crevecoeur, C. Electrical Conduction in Li-Doped CoO. *J. Phys. Chem. Solids* **1969**, 30, 1151–1160.
- (48) Scanlon, D. O.; Morgan, B. J.; Watson, G. W. Modeling the Polaronic Nature of *p*-Type Defects in Cu₂O: The Failure of GGA and GGA+U. *J. Chem. Phys.* **2009**, 131, 124703.
- (49) Huang, D.; Pan, Y. First-Principles Calculations of Intrinsic Defects in the *p*-Type Semiconductor CuAlO₂. *Can. J. Phys.* **2010**, 88, 927–932.
- (50) Roth, H.-F.; Meyer, G.; Hu, Z.; Günter, K. Synthesis, Structure, and X-Ray Absorption Spectra of Li_xNbO₂ and Na_xNbO₂ (x ≤ 1). *Z. Anorg. Allg. Chem.* **1993**, 619, 1369–1373.
- (51) Brennan, T. D.; Ibers, J. A. Lanthanum Orthosilicate Selenide, La₂SeSiO₄. *Acta Crystallogr. C* **1991**, 47, 1062–1064.
- (52) Wang, Z.; Nayak, P. K.; Caraveo-Frescas, J. A.; Alshareef, H. N. Recent Developments in *p*-Type Oxide Semiconductor Materials and Devices. *Adv. Mater.* **2016**, 28, 3831–3892.

(53) Zhang, K. H. L.; Xi, K.; Blamire, M. G.; Egdell, R. G. *P-Type Transparent Conducting Oxides*. *J. Phys.: Condens. Matter* **2016**, *28*, 383002.

(54) Keezer, R. C.; Bowman, D. L.; Becker, J. H. Electrical and Optical Properties of Lead Oxide Single Crystals. *J. Appl. Phys.* **1968**, *39*, 2062–2066.

(55) Nam, K. M.; Park, H. S.; Lee, H. C.; Meekins, B. H.; Leonard, K. C.; Bard, A. J. Compositional Screening of the Pb–Bi–Mo–O System. Spontaneous Formation of a Composite of *p*-PbMoO₄ and *n*-Bi₂O₃ with Improved Photoelectrochemical Efficiency and Stability. *J. Phys. Chem. Lett.* **2013**, *4*, 2707–2710.